Stress and Defect Effects on Electron Transport Properties at SnO$_2$/Perovskite Interfaces: A First-Principles Insight

Wenhua Pu, Wei Xiao,* Jianwei Wang, Xiao-Wu Li, and Ligen Wang

ABSTRACT: The structural and electronic properties of interfaces play an important role in the stability and functionality of solar cell devices. Experiments indicate that the SnO$_2$/perovskite interfaces always show superior electron transport efficiency and high structural stability even though there exists a larger lattice mismatch. Aiming at solving the puzzles, we have performed density-functional theory calculations to investigate the electronic characteristics of the SnO$_2$/perovskite interfaces with various stresses and defects. The results prove that the PbI$_2$/SnO$_2$ interfaces have better structural stability and superior characteristics for the electron transport. The tensile stress could move the conduction band minimum (CBM) of CH$_3$NH$_3$PbI$_3$ upward, while the compressive stress could move the CBM of SnO$_2$ downward. By taking into account the stress effect, the CBM offset is 0.07 eV at the PbI$_2$/SnO$_2$ interface and 0.28 eV at the MAI/SnO$_2$ interface. Moreover, our calculations classify V$_I$ and I$_i$ at the PbI$_2$/SnO$_2$ interface and Sn−I, I$_i$ and Sn$_i$ at the MAI/SnO$_2$ interface as harmful defects. The I$_i$ defects are the most easily formed harmful defects and should be avoided at both interfaces. The calculated results are in agreement with the available experimental observations. The present work provides a theoretical basis for improving the stability and photovoltaic performance of the perovskite solar cells.
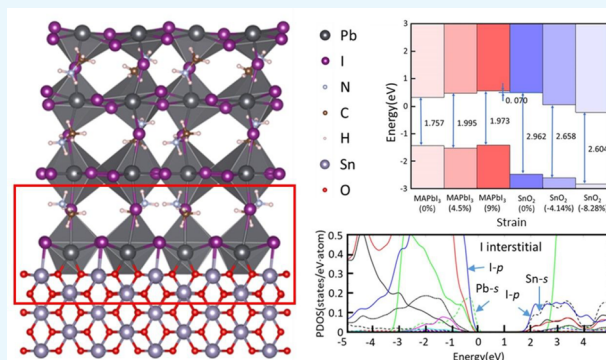
1. INTRODUCTION

Perovskites have been emerging as one of the important candidate materials for new photovoltaic cells because they possess superior photovoltaic performance of high light absorption coefficient, large carrier mobility, and long electron−hole diffusion length and also are easy to prepare in various synthetic methods with low manufacturing cost.[1−4] Perovskite organic metal halides were employed as a light harvester for the perovskite solar cells (PSCs) by Kojima et al. in 2009.[5] With the efforts of many researchers, the efficiency of perovskite-based solar cells has increased from 3.8% to 25.5%.[5−8] PSCs are generally composed of the transparent conductive electrodes, electron transport layers (ETLs), perovskite light absorption layers, hole transport layers (HTLs), and metal electrodes.[9] These layers are stacked together, and many interfaces are formed between the layers, all of which will affect the charge transport of the device. The bonding and defect properties of the interfaces play an important role in the interfacial stability and functionality. Therefore, it is very important to study the characteristics of the interfaces, which will help researchers overcome the shortcomings at the interfaces and continuously improve the efficiency of PSCs.

Electron transport layers are an important part of PSCs, which are responsible for transferring electrons to the electrodes. Electrons excited by light in the perovskite layer must transfer through the perovskite/ETL interfaces and then be collected by the ETL. Meanwhile, electrons and holes might recombine at the interfaces, which often affects the power conversion efficiency (PCE) of the device. TiO$_2$ is the most popular ETL used in PSCs because of its suitable conduction band minimum (CBM) and the history of being used as an ETL in dye sensitized solar cells.[10,11] The PCE of TiO$_2$-based PSCs has exceeded 25%.[12] However, the development of TiO$_2$ is limited by a serious disadvantage, that is, its electron transport speed is very low, only 0.1−0.4 cm^2 V s^{-1} and electrons are easy to accumulate at the TiO$_2$/perovskite interfaces.[13] Many other materials such as ZnO,[14] Zn$_2$SnO$_4$,[15] BaSnO$_3$,[16] SrTiO$_3$,[17] CdS,[18] CdSe,[19] WO$_3$,[20] In$_2$O$_3$,[21] Nb$_2$O$_5$,[22] and CeO$_x$[23] have been investigated as ETL with different strengths and weaknesses. In comparison, SnO$_2$ as the promising ETL has attracted wide attention in recent years, and the PCE of SnO$_2$-based PSCs has also exceeded 25%.[24]
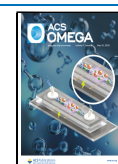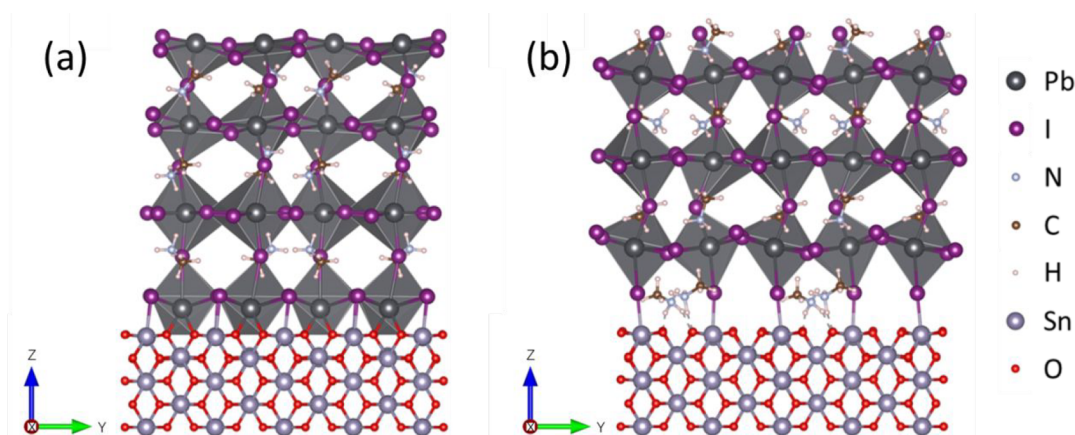
Figure 1. Optimized stable geometrical structures of SnO_2/perovskite interfaces: (a) PbI_2/SnO_2; (b) MAI/SnO_2.

SnO$_2$ has superior physical properties for being used as an ETL. Its electron transfer efficiency is much higher, reaching 240 cm^2 V s^{-1},[13] although it has a cell and band structure similar to those of TiO$_2$. The CBM of SnO$_2$ is lower than TiO$_2$, which is favorable for electronic transport.[25] Also, the larger band gap of SnO$_2$ makes it less susceptible to ultraviolet rays.[26] Moreover, SnO$_2$ can be prepared at low temperatures, which is more convenient and can be used in flexible solar cells.[27] In 2015, Li et al. were the first batch to use mesoporous SnO$_2$ films as ETL and got a PCE of 10.18%.[28] Ke et al. prepared SnO$_2$ thin films by thermal decomposition of SnCl$_2$·2H$_2$O precursor on fluorine doped tin oxide (FTO), and the yield PCE reached 17.21%.[29] Anaraki et al. obtained 20.7% PCE by the spin coating and chemical bath deposition method.[30] Jiang et al. fabricated planar PSCs with a certificated PCE of 23.32% by using the organic halide salt phenyl-ethylammonium iodide (PEAI) to passivate the surface defects of HC(NH$_2$)$_2$−CH$_3$NH$_3$ mixed perovskite films.[31] Recently, Yoo et al. tuned the chemical bath deposition of SnO$_2$ and got better ETL with ideal film coverage, thickness, and composition, which could be beneficial for the interface properties, and thus a certified PCE of 25.2% was finally obtained.[24]

Many experimenters have reached a consensus on the excellent performance of SnO$_2$ as an ETL and they have employed a lot of approaches to improve the properties of the SnO$_2$/perovskite interfaces.[32−35] Yang et al. found that the recombination rate of quantum dot SnO$_2$/perovskite interfaces is less than that of nanocrystalline SnO$_2$/perovskite interfaces.[26] Zhang et al. used density functional theory (DFT) and experiments to comprehensively investigate the interface structures and transport properties of the CH$_3$NH$_3$PbI$_3$/SnO$_2$ interfaces and found that the interface contacted by the PbI$_2$ layer is more stable than that contacted by the CH$_3$NH$_3$I layer.[34] In order to adjust the interfacial stress caused by the lattice mismatch, Du et al. introduced the amino acid self-assembled layer as the buffer layer, which improved the quality of perovskite films, enhanced the charge transfer/extraction at the interfaces, and finally made it achieve a PCE of 20.68%.[35] Kim et al. studied the orbital hybridization and the effects of O vacancy and Ti/Sn interstitial at TiO$_2$/perovskite and SnO$_2$/perovskite interfaces and indicated that SnO$_2$ is better than TiO$_2$ as an ETL material.[36] Until now the understanding of the influences of the microstructures on the performance of the SnO$_2$/perovskite interfaces, such as the stress produced by the

mismatch and the defect effects, is far from enough. So in this paper, we will carry out a systematic study on the structural and electronic properties of the SnO$_2$/perovskite interfaces. The remainder of the paper is organized as follows. In Section 2, the theoretical methods and the computational details are described. Section 3 presents the interfacial properties of the clean heterointerfaces, and the stress and defect effects on the electron transport at the interfaces are explored. Finally, a short summary is given in Section 4.

2. COMPUTATIONAL METHODS

The first-principles calculations in the framework of DFT were performed using Vienna ab initio Simulation Package (VASP).[37,38] The electron−ion interaction was described using the projector augmented wave method.[39,40] The energy cutoff for the plane wave basis set was 500 eV for all calculations. In the simulation, an empirical pairwise correction proposed by Grimme in terms of the DFT+D2 scheme had also been included for more precisely depicting the dispersion interactions in the systems.[41] For both bulk and interface systems, their structures were optimized by using the generalized gradient approximation (GGA) in the Perdew−Burke−Ernzerhof (PBE) form.[42] For the accuracy of the band alignment and electronic transport properties at the interfaces, the electronic properties were calculated using the Heyd−Scuseria−Ernzerhof screened Coulomb hybrid functional (HSE06).[43] The supercell parameters and the atomic positions were allowed to relax until the forces on all atoms were converged to 0.05 eV/Å.

The calculated parameters of bulk tetragonal CH$_3$NH$_3$PbI$_3$ (MAPbI$_3$) perovskites are a = 8.69 and c = 12.80 Å, which match well with the previous DFT calculations and experimental observations.[44−46] In order to build a typical SnO$_2$/perovskite interface, we also optimized the lattice constants of SnO$_2$ to be a = 4.83 and c = 3.24 Å, which are in good agreement with other researches.[47,48] Then, we constrained the lattice constants of the perovskite slab with these of the SnO$_2$ slab, which is always employed as the substrate in experiments. Haruyama et al. listed all possible surface of tetragonal CH$_3$NH$_3$PbI$_3$, and we chose the (001) surface to stack interface models because the (001) surface has the best match with the SnO$_2$ lattice.[49] Due to the structural characteristics of the (001) slab of perovskites, we produced two kinds of interfaces based on the different terminations: the MAI termination with MA$^+$ and I$^-$ ions and the PbI$_2$

termination with Pb^{2+} and I^- ions, as shown in Figure 1. The heterointerfaces were built by connecting the five-layer SnO_2 slabs with seven-layer perovskite slabs together and left 20 Å vacuum along the nonperiodic direction. The SnO_2 slab contains 10 SnO_2 units, namely, 60 atoms. The perovskite slab contains 6.5 $MAPbI_3$ units with 78 atoms for PbI_2 termination, and 7.5 $MAPbI_3$ units with 90 atoms for MAI termination. The bottom atoms of the SnO_2 substrate were fixed to keep the bulk environment. The corresponding k-point mesh was $4 \times 4 \times 1$.

3. RESULTS AND DISCUSSION

3.1. Stability and Bonding Characteristics of SnO_2/Perovskite Interfaces. In order to evaluate the stability of the SnO_2/perovskite interfaces, we calculate the interfacial adhesion energy (E_{ad}), which is defined as

$$E_{ad} = -(E_{interface} - E_{SnO_2} - E_{perovskite})/S \quad (1)$$

where $E_{interface}$, E_{SnO_2}, and $E_{perovskite}$ denote the total energies of the heterointerface supercell, the SnO_2 substrate and the perovskite slab, respectively and S is the area of the interfaces. The slabs of SnO_2 and perovskite are constrained to match the lattice constants at the interfaces. A positive interfacial adhesion energy implies that it is energetically favorable to form the interface.

By using eq 1, we have obtained that the PbI_2/SnO_2 interfaces have higher interfacial adhesion energy of 1.22 J/m^2 as shown in Table 1. For the MAI/SnO_2 interfaces, it is

Table 1. Calculated Interfacial Adhesion Energy, Lattice Mismatch and Bader Charge of Different SnO_2/Perovskite Interfaces

interface	interfacial adhesion energy (J/m^2)	lattice mismatch (%)	Bader charge (e)
$PbI_2/$ SnO_2	1.22	11	0.74
$MAI/$ SnO_2	0.66	11	0.54

only 0.66 J/m^2. These results show that the PbI_2/SnO_2 interfaces are more stable than the MAI/SnO_2 interfaces. Since perovskites are supposed to grow on the SnO_2 surface in experiments, their lattice constants parallel to the interface are compressed to match SnO_2. Then, we calculated the lattice mismatch of the SnO_2/perovskite heterointerfaces to be about 11% (Table 1), larger than that (7.35%) of TiO_2/perovskite heterointerfaces. However, compared to the stable PbI_2/TiO_2 interfaces (0.93 J/m^2), the SnO_2/perovskite interface is energetically more stable even though it has a large mismatch.[50] But when referred to the heterointerfaces of traditional CZTS/CdS solar cells (3.05 J/m^2), it can be deduced that the binding at the SnO_2/perovskite interfaces is still relatively weak.[51]

In order to study why the stability of the PbI_2/SnO_2 interface is better, we continue to study the bonding characteristics at SnO_2/perovskite interfaces from the atomic and electronic levels. First, the analyses of Bader charge are listed in Table 1 to address the interactions between two slabs. It shows that for the PbI_2/SnO_2 interfaces, the perovskite slab lost more electron (0.74 e) than the MAI/SnO_2 interfaces (0.54 e). With more electron transfer between the two slabs, the binding of the PbI_2/SnO_2 interfaces might be stronger.

Second, the proportion of bonded atoms of the perovskite surface and bond length of the interface structures are obtained in Table 2. The bonding ratio of one kind of bond is defined as

Table 2. Proportion of Bonded Atoms of the Perovskite Surface and Bond Length of Interface Structures

interface	bond (Pb−O or H−O)		bond (Sn−I)	
	bond number (%)	band length (Å)	bond number (%)	bond length (Å)
$PbI_2/$ SnO_2	50	2.29	100	2.82−2.94
$MAI/$ SnO_2	37.5	1.41−1.63	50	2.87

the surface chemical bond/surface atom number (O and Sn). In the PbI_2 termination, the bonding ratio of Pb−O bonds is 50%, and the bond length of Pb−O is 2.29 Å. For Sn−I bonds, the bonding ratio is 100% and the bond length is 2.82−2.94 Å. In the MAI termination, H−O and Sn−I bonds dominate the stability of the interfaces, and the bonding ratios (bond length) are 37.5% (1.41−1.63 Å) and 50% (2.87 Å), respectively. On the basis of the above analyses of the atomic structures at the interfaces, we can conclude that the PbI_2/SnO_2 interfaces not only have more atoms bonded but also contain some Pb−O bonds with high strength when compared to the MAI/SnO_2 interfaces, which can be considered another strong evidence for its high interfacial adhesion energy.

Furthermore, the charge density differences at the interfaces are given to clarify the interactions of different atoms. Figure 2 depicts the charge density differences (left panels) and planar-averaged charge density differences (right panels) of the two interfaces. We can clearly observe the strong Pb−O and Sn−I coupling at the PbI_2/SnO_2 interfaces, while only some Sn−I coupling at the MAI/SnO_2 interfaces. Electrons are favorable to accumulate around O and I atoms (yellow region) and deplete around Sn and Pb atoms (green region). The weak charge transfer at the MAI/SnO_2 interfaces can also be quantitatively described by the planar-averaged charge density differences along the Z direction. The charge distribution at the interfaces could form an internal electric field to affect the charge transport properties of the solar cells. Thus, more stable PbI_2/SnO_2 interfaces are supposed to cause a stronger internal electric field and make the electron−hole pairs separate more easily at the interfaces.[52] We can speculate that the PbI_2/SnO_2 interfaces could be easier to form during the device manufacturing process as evidenced by experiments,[53] and it is beneficial to the performance improvement of the electron transport.

3.2. Characteristics of the Electron Transport at SnO_2/Perovskite Interfaces. The electrical properties at the interfaces are closely related to the electron transport at the interfaces. In order to understand the electrical properties of SnO_2/perovskite interfaces, we first resorted to the partial density of states (PDOSs) of the interfaces, as shown in Figure 3. It can be seen from Figure 3 that the CBM of SnO_2 at two different interfaces are all significantly lower than that of perovskites. Because with a proper band gap, perovskites always act as the light absorption layer, electrons should be excited from the top of the valence band maximum (VBM) (I-p and Pb-s orbitals) of perovskites to the conduction band minimum (CBM) of perovskites (Pb-p orbitals) and then transferred from the conduction bands of the perovskites to the conduction bands of SnO_2 (Sn-s orbitals). It also clearly shows
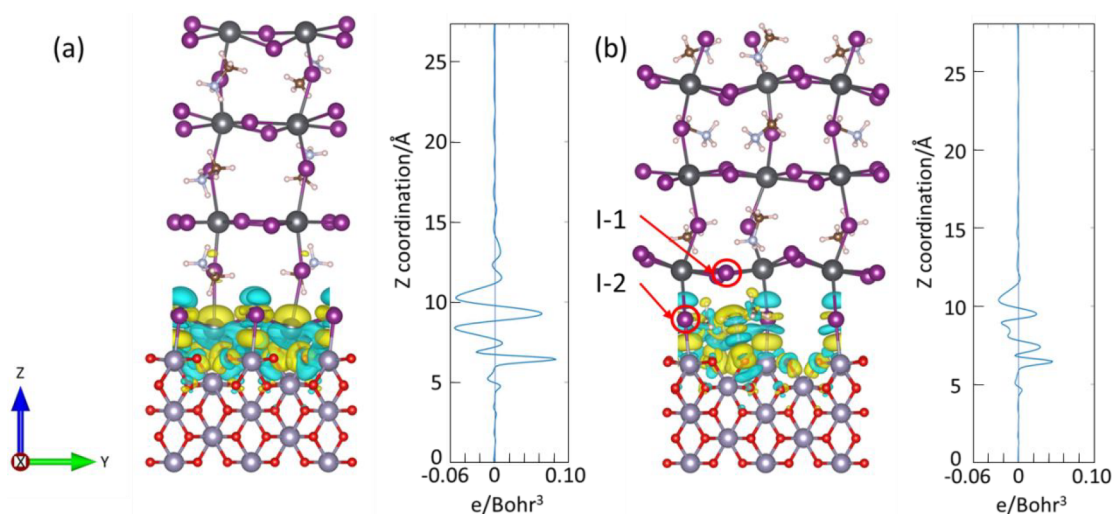
Figure 2. Main views of the 3D charge density differences (left panels) and planar-averaged charge density differences (right panels) along the Z direction of the (a) PbI_2/SnO_2 and (b) MAI/SnO_2 interfaces, respectively. The location of two different defects I-1 and I-2 at the latter interfaces are also marked. The yellow region denotes the electron accumulation, and the green region represents the electron depletion.
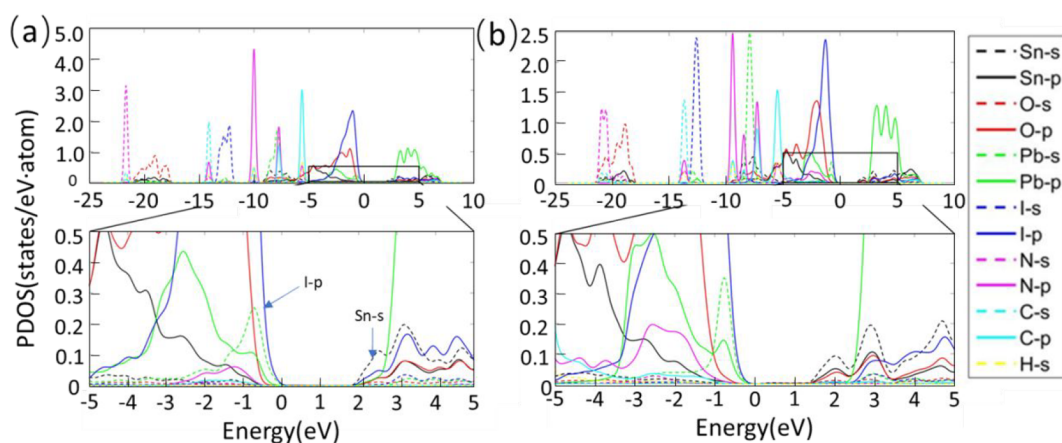

Figure 3. Partial density of states (PDOSs) for the upper and lower two-layer atoms at the (a) PbI_2/SnO_2 and (b) MAI/SnO_2 interfaces.

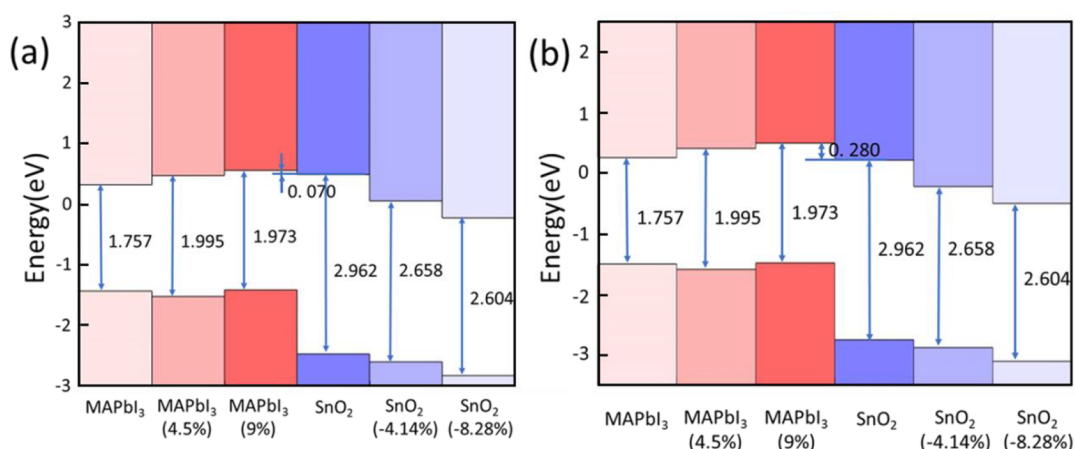**Figure 4.** CBM and VBM of the (a) PbI_2/SnO_2 and (b) MAI/SnO_2 interfaces with their deformation rates in brackets below.

that MA molecules have little effect on CBM and VBM at the interfaces and almost no participation in electron transport. By comparing the band gaps of the two interfaces by the HSE06, it can be found that that the band gap of the PbI_2/SnO_2 (1.76 eV) interface is slightly smaller than that of the MAI/SnO_2 interface (2.26 eV). This is because the outflow of electrons

from the Pb atoms causes the Pb states to shift to the left, thereby reducing the band gap.[54] The band gap of the PbI_2/SnO_2 interfaces is closer to the ideal one of single-junction solar cells, which indicates that the PCE of the PbI_2/SnO_2 interfaces might be higher. Moreover, the rate of electron transport at the interfaces can be determined by the CBM

difference between the perovskite and SnO_2 layers. A larger energy difference could accelerate the electron transport. Thus, comparing the positions of Pb-p and Sn-s orbitals in Figure 3, we can safely say that the electron transport at the MAI/SnO_2 interfaces could have a higher efficiency. To deeply understand the characteristics of the electronic transport at the interfaces, the stress and defect effects will be further discussed in the following.

3.2.1. Stress Effect on the Electronic Transport at SnO_2/Perovskite Interfaces. Because of the lattice mismatch between the perovskite and SnO_2 layers, there necessarily exists stress at the interfaces. The stress could have a nonnegligible impact on the electron transport at the interfaces and therefore should be taken into account. Figure 4 shows the CBM and VBM of the perovskite and SnO_2 layers under different deformation rates, where positive and negative values indicate that the material bears tensile stress and compressive stress, respectively. We considered the following situations: (1) all the deformation caused by the lattice mismatch occurred on the perovskite layer and it was subjected to tensile strain at the deformation rate of 9%; (2) all the deformation was applied on the SnO_2 layer and it was subjected to compressive strain at the deformation rate of −8.28%; (3) the deformation was equally applied to the perovskite and SnO_2 layers, and the deformation rate of the perovskite and SnO_2 layers is 4.5% and −4.14%, respectively. The deformation rate here refers to the degree of deformation of the matched lattice constant at the interfaces relative to the initial lattice constant. The cell volume remains unchanged under different conditions of deformation. The core level alignment method has been employed to obtain the band alignment of two different SnO_2/perovskite interfaces by using the PBE-HSE functional.[55,56] From Figure 4, we can see for both PbI_2/SnO_2 and MAI/SnO_2 interfaces, the CBM of perovskite is uplifted gradually under the tensile stress and the corresponding band gap increases; the CBM of SnO_2 is decreased gradually under the compressive stress with a reduced band gap. When the deformation at the interfaces mainly occurs on the perovskite layer, the CBM difference between the perovskite and SnO_2 is relatively small, i.e., 0.07 eV at PbI_2/SnO_2 interfaces and 0.28 eV at MAI/SnO_2 interfaces, which could be beneficial to improve the PCE of the PSCs;[57,58] when the SnO_2 layer carries all the deformation at the interfaces, the CBM difference between the two layers could be enlarged, i.e., 0.55 eV at PbI_2/SnO_2 interfaces and 0.76 eV at MAI/SnO_2 interfaces, which is conducive to improve the electron transport efficiency at the interfaces.[54,59] From Figure 4, it can be also found that the CBM offset between the two layers at the MAI/SnO_2 interfaces is greater than that at the PbI_2/SnO_2 interfaces, indicating that the MAI/SnO_2 interfaces might be more suitable for electron transport. As in the preparation process of PSCs, $MAPbI_3$ always grows on the SnO_2 layer, the perovskite layer is supposed to withstand the major deformation caused by the lattice mismatch at the interfaces. By considering the stress effect, we find that for the PSCs the CBM offset at the PbI_2/SnO_2 interfaces is close to 0.07 eV, and at the MAI/SnO_2 interfaces is approximately 0.28 eV. There are many researchers measuring the CBM offset at perovskite/SnO_2 interfaces in the experiments. For example, Park et al. and Chen et al. measured the optical properties of SnO_2/$CH_3NH_3PbI_3$ heterojunction by the ultraviolet–visible spectrophotometer, and they both showed the difference was 0.27 eV.[60,61] Yang et al. measured the Fermi level by Kelvin probe force microscopy

(KPFM) and obtained the value of 0.10 eV,[62] and Xiong et al. measured the VBM and CBM of SnO_2 by the UV photoelectron spectroscopy (UPS) and speculated it to be 0.30 eV.[63] The predicted values by the high accurate HSE06 method are very consistent with the experimental results, and our theoretical calculations have proved that the stress can be used to adjust the PCE and the electron transport efficiency at the interfaces.[64,65]

3.2.2. Defect Effect on the Electronic Transport at SnO_2/Perovskite Interfaces. Defects are more likely to occur at the interfaces, and the produced defects are likely to affect the electron transport properties at the interfaces. Therefore, we have studied the formation of several defects that may occur at the two types of interfaces and analyzed their influence on the electron transport properties at the interfaces. The formula for calculating defect formation energy is shown in eq 2.

$$E_f = E_d - E_{SC} - \sum_i n_i \mu_i \tag{2}$$

E_d and E_{SC} are the total energies of the defect system and defect-free supercell structure, respectively. μ_i and n_i are the chemical potentials and the number of defect species i that have been added to ($n_i > 0$) or removed from ($n_i < 0$) the supercell structure. When the number of all the species in the supercell does not change, such as antisite substitutions, then $n_i = 0$.

The formation energies of defects depend on the chemical potentials (μ_i) of the constituent elements in preparation environments. In this work, we use the chemical potentials at the point B ($\Delta\mu_{Pb} = -1.06$ eV, $\Delta\mu_i = -0.6$ eV, $\Delta\mu_{MA} = -2.41$ eV) mentioned by Yin's work as a reference, which is an intermediate state for the growth of the perovskites.[66] $\Delta\mu_i$ and μ_i are linked by

$$\Delta\mu_i = \mu_i - \mu_i^{ref} \tag{3}$$

where μ_i^{ref} is the chemical potential of the most stable elemental phase.

For the defects related with SnO_2, the relevant chemical potentials μ_{Sn} and μ_O can be determined by the following formula:

$$\Delta\mu_{Sn} + 2\Delta\mu_O = \Delta H(SnO_2) = -4.77 eV \tag{4}$$

where $\Delta H(SnO_2)$ is the formation enthalpy of SnO_2. Here, we continue to employ an intermediate state ($\Delta\mu_o^{med}$ and $\Delta\mu_{Sn}^{med}$) as the growth condition, which is the average value of the two extreme environments, namely, O-richest (Sn-poorest) and O-poorest (Sn-richest) conditions. In the former case, $\Delta\mu_o^{rich} = 0$, and the corresponding Sn-poorest chemical potential $\Delta\mu_{Sn}^{poor}$ can be obtained by eq 4. In the latter case, the O-poorest chemical potential $\Delta\mu_o^{poor}$ can be obtained through eq 4 by setting $\Delta\mu_{Sn}^{rich} = 0$. On the basis of the above, we compute $\Delta\mu_o^{med} = -1.19$ eV and $\Delta\mu_{Sn}^{med} = -2.39$ eV, for the intermediate state. Therefore, the related defect formation energies by using the chemical potentials ($\Delta\mu_o^{med}$ and $\Delta\mu_{Sn}^{med}$) can be derived.

In previous studies, Yin et al.'s DFT calculations demonstrated that V_{Pb}, V_I, I_i, V_{MA} and MA_{Pb} defects with low formation energies have transition levels less than 0.05 eV above (below) VBM (CBM) in $CH_3NH_3PbI_3$.[66] Freeman et al. found that the point defects in SnO_2 are mainly Schottky defects, and the interstitial defects Sn_i and O_i are easily formed.[67] Noh et al. found there are a lot of oxygen vacancies in SnO_2 films.[68] Shi et al. indicated that there might be some

Table 3. Defect Formation Energies at the PbI$_2$/SnO$_2$ Interfaces

	defect								
	Sn−I	V$_I$	V$_{MA}$	V$_O$	I$_i$	MA$_{Pb}$	O$_i$	Pb−O	Sn$_i$	V$_{Pb}$
formation energy (eV)	2.20	**0.37**	1.58	**0.10**	**0.26**	**−0.60**	1.37	2.69	**−0.21**	3.60

element exchanges at the interfaces.[69] On the basis of these results, we have considered all these possible point defects that might be easily formed at the CH$_3$NH$_3$PbI$_3$/SnO$_2$ interfaces, including four vacancies (V$_O$, V$_{Pb}$, V$_I$, V$_{MA}$), three interstitials (Sn$_i$, O$_i$, I$_i$), one cation substitution (MA$_{Pb}$), and two antisite substitutions (Sn−I, Pb−O). Table 3 lists the formation energies of ten possible defects at the PbI$_2$/SnO$_2$ interfaces. Among these defects, these five types of defects, such as V$_I$, V$_O$, I$_i$, MA$_{Pb}$, and Sn$_i$ are more likely to form at the interfaces with a formation energy less than 1 eV. V$_O$ has a low formation energy of 0.10 eV, which is consistent with the previous experiments' observations that O vacancy can easily form at the interface.[68,69] For V$_I$ and I$_i$, their formation energies at the interface are 0.37 and 0.26 eV, respectively, relatively smaller when compared to the bulk. It can be attributed to the bonding environment at the interface that the lattices of the perovskites are expanded by the tensile stress, which weakens the bond strength of Pb−I bonds and enlarges the interstice space. Therefore, V$_I$ and I$_i$ become easily formed at the interface. For the MA$_{Pb}$, the formation energy at the interface is largely reduced to −0.60 eV. By checking the bonding characteristics, we can observe that the MA loses an H to form CH$_3$NH$_2$, and the H preferably passivates the dangling bonds of O atoms at the interface, which largely reduces the formation energy of MA$_{Pb}$. [See Figure S1.] Similarly, one interstitial Sn atom could form two strong Sn−O bonds at the interface, which makes the formation energy of Sn$_i$ much lower than the bulk. However, it is worth noting that the free volume and the dangling O atoms might be exhausted by a small content of defects, and then the interstitial defects could become hard to form.

In order to address the impact of the defects on the electron transport efficiency at the PbI$_2$/SnO$_2$ interface, the PDOSs of these five defect systems by the HSE06 method have been depicted in Figure 5. From Figure 5a, we can see the formation of V$_I$ at the interfaces causes Pb-p states slightly shift to the left, which reduces the band gap and makes the CBM of CH$_3$NH$_3$PbI$_3$ significantly lower than that of SnO$_2$. Therefore, the electron transport from CH$_3$NH$_3$PbI$_3$ to SnO$_2$ becomes denpendent on thermal effects. For V$_O$ at the interface, it almost has little effect on the band gap, VBM and CBM (Figure 5b), which demonstrates that a small amount of oxygen vacancies at the interface might be acceptable. As for I$_i$ at the interface, it causes I-p states to shift slightly to the left (Figure 5c), which is close to or just below the CBM of SnO$_2$. To some extent, it could also affect the electron transport mechanism at the interface. For Sn$_i$ at the interfaces, we can observe a shallow defect level (Sn-s) lying at $E = -0.7$ eV below the VBM (Figure 5d). The shallow defect level caused by Sn$_i$ could not become the recombination center of electrons and holes and might not be harmful for the electron transport at the interfaces. The formation of MA$_{Pb}$ at the interface causes the Pb-p states slightly shift to the right (Figure 5e); this does not affect the transport mechanism of electrons but may cause electrons accumulation at the interface. This change could increase the open circuit voltage of the PSCs, which finally affects the PCE of solar cells.[70]
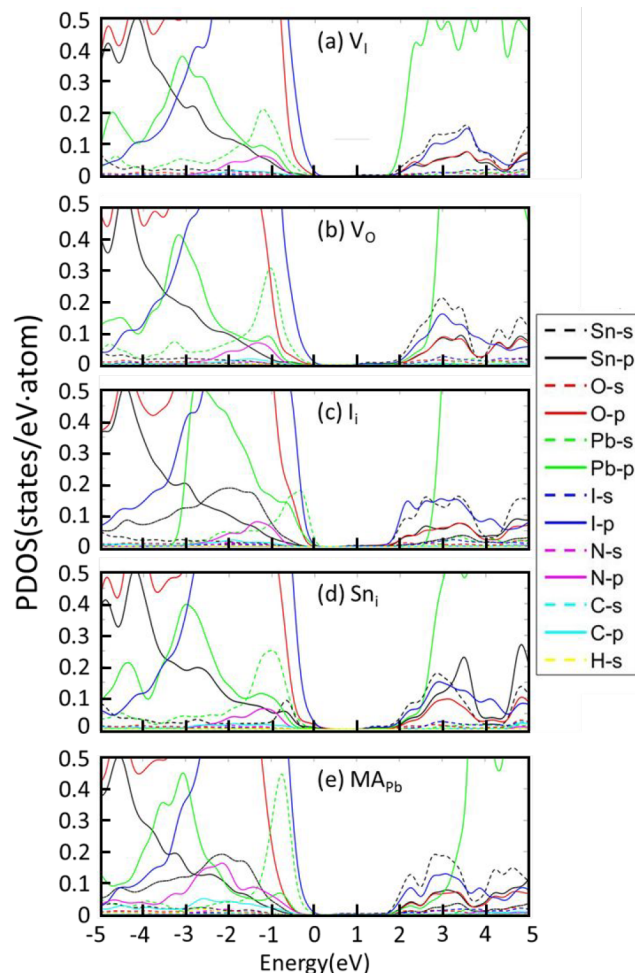

Figure 5. PDOSs for the upper and lower two-layer atoms at the PbI$_2$/SnO$_2$ interfaces with different defects: (a) I vacancy, (b) O vacancy, (c) I interstitial, (d) Sn interstitial, and (e) MA$_{Pb}$ cation substitution.

As for the MAI/SnO$_2$ interfaces, we have also chosen several possible point defects including five vacancies (V$_O$, V$_{Pb}$, V$_{I-1}$, V$_{I-2}$, V$_{MA}$), three interstitials (Sn$_i$, O$_i$, I$_i$), one cation substitution (MA$_{Pb}$), and one antisite substitution (Sn−I).[66−69] Table 4 lists the corresponding formation energies of these possible defects. Due to the different bonding environments at the MAI/SnO$_2$ interfaces, two different iodine atoms labeled as I-1 and I-2 in Figure 2 are involved in this study. Among these ten defects, eight types of defects have a formation energy less than 1 eV, namely, Sn−I, V$_{I-1}$, V$_{I-2}$, V$_O$, I$_i$, MA$_{Pb}$, O$_i$, and Sn$_i$. Obviously, compared to the defects at the PbI$_2$/SnO$_2$ interfaces, Sn−I, V$_O$, I$_i$, O$_i$, and Sn$_i$ at the MAI/SnO$_2$ interfaces are favorable to form with a relatively smaller formation energy. We can attribute these to the poor stability and bonding characteristics of the MAI/SnO$_2$ interfaces. The Sn−I antisite substitution becomes easily formed at this weak-binding interface with the formation energy of 0.89 eV. For the defect of I vacancy, the formation energy of V$_{I-2}$ (0.33 eV) is

Table 4. Defect Formation Energies at the MAI/SnO₂ Interfaces

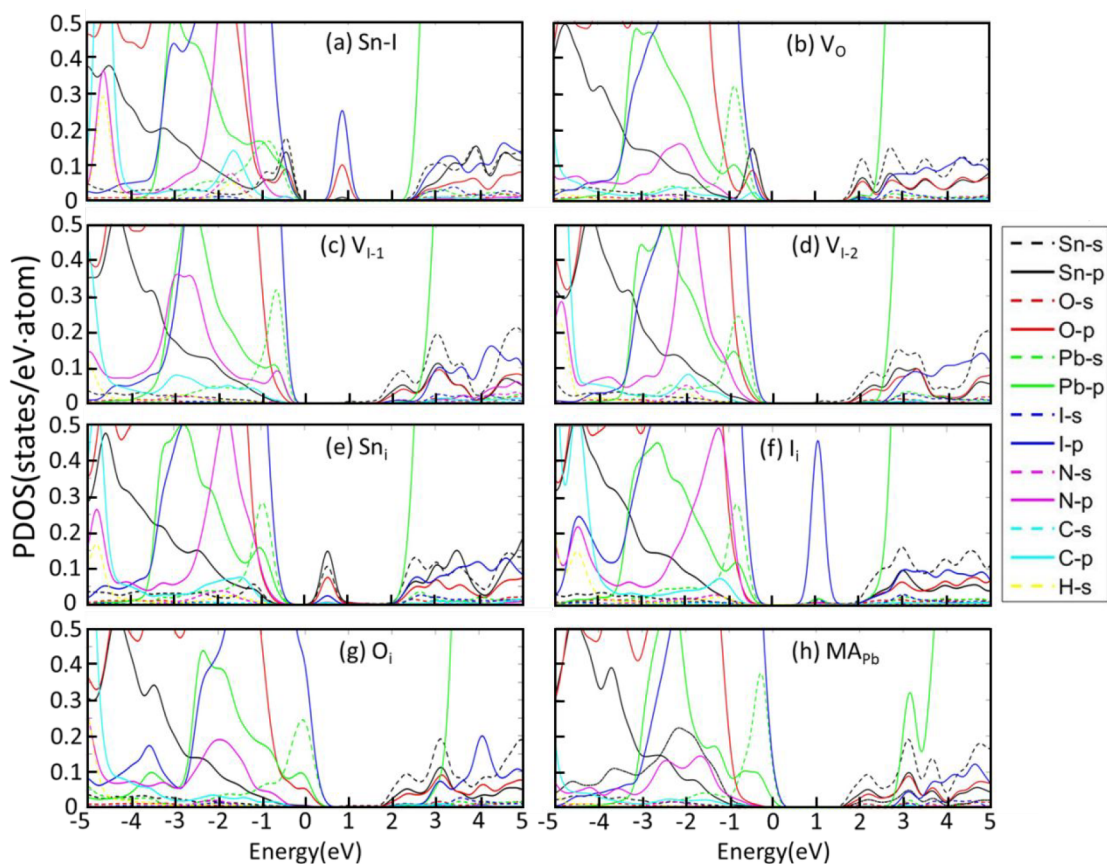|	defect									
	Sn–I	V_{I-1}	V_{I-2}	V_{MA}	V_O	I_i	MA_{Pb}	O_i	Sn_i	V_{Pb}
formation energy (eV)	0.89	0.63	0.33	1.91	0.01	0.11	0.17	0.79	−0.32	1.86

Figure 6. PDOSs for upper and lower two-layer atoms at the MAI/SnO₂ interfaces with different defects: (a) Sn–I antisite substitution, (b) O vacancy, (c) I-1 vacancy, (d) I-2 vacancy, (e) I interstitial, (f) Sn interstitial, (g) O interstitial, and (h) MA_{Pb} cation substitution.

less than that of V_{I-1} (0.63 eV), because the strength of Sn–I bonds is weaker than that of Pb–I bonds. V_O has a low formation energy of 0.01 eV at the MAI/SnO₂ interfaces, which is similar to that for the PbI₂/SnO₂ interfaces and consistent with experimental observations.[67,68] Compared with the PbI₂/SnO₂ interfaces, the formation energies of I_i and O_i are becoming lower. This is because the MAI/SnO₂ interfaces have larger interstice space at the interfaces. For MA_{Pb} at the MAI/SnO₂ interfaces, its formation energy becomes larger due to that the MA molecule replacing a Pb atom is far away from the SnO₂ layer and could not be bonded to the dangling O atom. As for Sn_i at the MAI/SnO₂ interfaces, we could also observe the similar phenomenon as the PbI₂/SnO₂ interfaces. It has very low formation energy of −0.32 eV because of the free volume and the dangling O atoms. [See Figure S2].

For these defects that might form at the MAI/SnO₂ interfaces, we also give the PDOSs in Figure 6 for further discussing their effects on the electron transport. From Figure 6a, it is noticed that there appear I-*p* and O-*p* levels near the middle of the band gap for the Sn–I antisite substitution defect. The deep levels in the band gap produced by the defect could attract electrons/holes and act as Shockley–Reid–Hall nonradiative recombination centers, which could adversely affect the efficiency of the solar cells. On the other hand, the band edges of VBM and CBM are totally changed, which are not conducive to electron transfer from CH₃NH₃PbI₃ to SnO₂. In Figure 6b, V_O creates a defect level (Sn-*s*) at E = −0.4 eV, where the level is located just above the VBM of CH₃NH₃PbI₃. Because the electronic transport path does not involve the VBM of SnO₂, the production of an oxygen vacancy could have no impact on the electron transport properties at the interfaces. From Figure 6c,d, we can see I-1 and I-2 vacancy defects have slightly moved the CBM of SnO₂ upward and have little effect on the electron transport process at the interfaces. For Sn_i and I_i defects, they both create defect levels near the middle of the band gap. As shown in Figure 6e,f, the defect levels are composed of Sn-*s*, Sn-*p*, O-*p*, and I-*p* at E = 0.5 eV for Sn_i and I-*p* and Pb-*p* at E = 1.1 eV for I_i, respectively. Thus, Sn_i and I_i can be classified as harmful defects and the deep levels might become recombination centers for electrons and holes. Besides, Sn_i makes the Pb-*p* shift to the CBM edge, which seriously influences the electron transfer from CH₃NH₃PbI₃ to SnO₂. Unlike other defects, O_i at the interfaces does not create any defect levels but narrows the band gap of SnO₂ to 1.58 eV as observed from Figure 6g. The reduced band gap could decrease the open circuit voltage of PSCs and therefore affects the PCE of the solar cells.[70] As for MA_{Pb} at the interfaces, it creates a defect level (Pb-*p*) at E = 3.2 eV (Figure 6h). As the

defect level is just located above the CBM of $CH_3NH_3PbI_3$, the effects on the electron transport can be neglected.

In general, V_I and I_i can be classified as the harmful defects, and V_O, Sn_i, and MA_{Pb} are the benign defects at the PbI_2/SnO_2 interfaces. At the MAI/SnO_2 interfaces, $Sn-I$, I_i, and Sn_i are harmful, and V_O, V_I, O_i, and MA_{Pb} are benign. Obviously, harmful defects are more easily formed at the MAI/SnO_2 interfaces. I_i is the most easily formed harmful defect at both PbI_2/SnO_2 and MAI/SnO_2 interfaces, which is consistent with the previous calculations and experimental results.[71−73] The harmful defects affect the transport of electrons from $CH_3NH_3PbI_3$ to SnO_2 or create deep levels that could become the recombination center of electrons/holes, thereby injuring the performance of PSCs. Therefore, minimizing the formation of the MAI/SnO_2 interfaces and avoiding the harmful defects could be beneficial to achieve high-performance and stable PSCs.

4. CONCLUSION

In this paper, first-principles calculations have been performed to study structural and electronic properties of $CH_3NH_3PbI_3$/SnO_2 interfaces by involving two different terminations (PbI_2 and MAI). It is expected that the PbI_2/SnO_2 interfaces have a high interfacial adhesion energy of 1.22 J/m^2 due to the interfacial $Pb-O$ and $Sn-I$ bonding as well as a stronger internal electric field for the electron−hole pairs separation. The effects of the stress and defects at the interfaces on the electron transport are also thoroughly addressed. The tensile stress could move the CBM of $CH_3NH_3PbI_3$ upward, and the compressive stress could move the CBM of SnO_2 downward. By considering the stress effect, the CBM offset at the PbI_2/SnO_2 interfaces is close to 0.07 eV, and at the MAI/SnO_2 interfaces is approximately 0.28 eV. Moreover, according to our research on possible interface defects, V_I, and I_i can be classified as the harmful defects at the PbI_2/SnO_2 interfaces, and $Sn-I$, I_i and Sn_i are harmful at the MAI/SnO_2 interfaces. The harmful defects affect the transport of electrons from $CH_3NH_3PbI_3$ to SnO_2 or create deep levels that could become the recombination center of electrons/holes. For both PbI_2/SnO_2 and MAI/SnO_2 interfaces, I_i is the most easily formed harmful defect and should be avoided in experiments. These results might contribute to the understanding of the $CH_3NH_3PbI_3$/SnO_2 interfaces and provide some references for finding ways to improve the stability and photovoltaic performance of the PSCs.

■ ASSOCIATED CONTENT

ⓢ Supporting Information

The Supporting Information is available free of charge at https://pubs.acs.org/doi/10.1021/acsomega.2c01584.

Figure S1, optimized stable geometrical structures of MA_{Pb} at PbI_2/SnO_2 interfaces; Figure S2, optimized stable geometrical structures of Sn_i at MAI/SnO_2 interfaces (PDF)

■ AUTHOR INFORMATION

Corresponding Author

Wei Xiao − *State Key Laboratory of Nonferrous Metals and Processes, GRINM Group Co., Ltd., Beijing 100088, PR China; GRIMAT Engineering Institute Co., Ltd., Beijing 101407, PR China; General Research Institute for Nonferrous Metals, Beijing 100088, PR China;* ◉ orcid.org/0000-0001-9447-3279; Email: xiaowei@grinm.com

Authors

Wenhua Pu − *State Key Laboratory of Nonferrous Metals and Processes, GRINM Group Co., Ltd., Beijing 100088, PR China; GRIMAT Engineering Institute Co., Ltd., Beijing 101407, PR China; General Research Institute for Nonferrous Metals, Beijing 100088, PR China; Department of Materials Physics and Chemistry, School of Materials Science and Engineering, Key Laboratory for Anisotropy and Texture of Materials, Ministry of Education, Northeastern University, Shenyang 110819, PR China*

Jianwei Wang − *State Key Laboratory of Nonferrous Metals and Processes, GRINM Group Co., Ltd., Beijing 100088, PR China; GRIMAT Engineering Institute Co., Ltd., Beijing 101407, PR China; General Research Institute for Nonferrous Metals, Beijing 100088, PR China*

Xiao-Wu Li − *Department of Materials Physics and Chemistry, School of Materials Science and Engineering, Key Laboratory for Anisotropy and Texture of Materials, Ministry of Education, Northeastern University, Shenyang 110819, PR China;* ◉ orcid.org/0000-0002-0238-9107

Ligen Wang − *State Key Laboratory of Nonferrous Metals and Processes, GRINM Group Co., Ltd., Beijing 100088, PR China; GRIMAT Engineering Institute Co., Ltd., Beijing 101407, PR China; General Research Institute for Nonferrous Metals, Beijing 100088, PR China*

Complete contact information is available at:
https://pubs.acs.org/10.1021/acsomega.2c01584

Notes

The authors declare no competing financial interest.

■ REFERENCES

(1) Glunz, S. W.; Feldmann, F.; Richter, A.; Bivour, M.; Hermle, M. The irresistible charm of a simple current flow pattern − 25% with a solar cell featuring a full-area back contact. *31st European Photovoltaic Solar Energy Conference.* **2015**, 259−263.

(2) Conings, B.; Drijkoningen, J.; Gauquelin, N.; Babayigit, A.; D'Haen, J.; D'Olieslaeger, L.; Ethirajan, A.; Verbeeck, J.; Manca, J.; Mosconi, E.; Angelis, F. D.; Boyen, H. G. Intrinsic thermal instability of methylammonium lead trihalide perovskite. *Adv. Energy Mater.* **2015**, *5* (15), 1500477.

(3) Kulbak, M.; Cahen, D.; Hodes, G. How Important Is the Organic Part of Lead Halide Perovskite Photovoltaic Cells? Efficient $CsPbBr_3$ Cells. *J. Phys. Chem. Lett.* **2015**, *6* (13), 2452−2456.

(4) Eperon, G. E.; Maria, P. G.; Sutton, R. J.; Andrea, Z.; Amir, H.; Franco, C. Inorganic caesium lead iodide perovskite solar cells. *J. Mater. Chem. A* **2015**, *3* (39), 19688−19695.

(5) Kojima, A.; Teshima, K.; Shirai, Y.; Miyasaka, T. Organometal halide perovskites as visible-light sensitizers for photovoltaic cells. *J. Am. Chem. Soc.* **2009**, *131* (17), 6050−6051.

(6) Berry, J.; Buonassisi, T.; Egger, D. A.; Hodes, G.; Kronik, L.; Loo, Y. L.; Lubomirsky, I.; Marder, S. R.; Mastai, Y.; Miller, J. S.; Mitzi, D. B.; Paz, Y.; Rappe, A. M.; Riess, I.; Rybtchinski, B.; Stafsudd, O.; Stevanovic, V.; Toney, M. F.; Zitoun, D.; Kahn, A.; Ginley, D.; Cahen, D. Hybrid Organic−Inorganic Perovskites (HOIPs): Opportunities and Challenges. *Adv. Mater.* **2015**, *27* (35), 5102−12.

(7) Yang, W. S.; Jung, E. H.; Jeon, N. J.; Kim, Y. C.; Lee, D. U.; Shin, S. S.; Seo, J.; Kim, E. K.; Noh, J. H.; Seok, S. I. Iodide management in formamidinium-lead-halide–based perovskite layers for efficient solar cells. *Science.* **2017**, *356* (6345), 1376–1379.

(8) NREL. Best Research-Cell Efficiencies. https://www.nrel.gov/pv/cell-efficiency.html.

(9) Xing, G.; Mathews, N.; Sun, S.; Lim, S. S.; Lam, Y. M.; Grätzel, M.; Mhaisalkar, S.; Sum, T. C. Long-Range Balanced Electron- and Hole-Transport Lengths in Organic-Inorganic $CH_3NH_3PbI_3$. *Science* **2013**, *342* (6156), 344–347.

(10) Qureshi, M.; Chetia, T. R.; Ansaria, M. S.; Sonib, S. S. Enhanced photovoltaic performance of meso-porous SnO_2 based solar cells utilizing 2D MgO nanosheets sensitized by a metal-free carbazole derivative. *J. Mater. Chem. A* **2015**, *3* (8), 4291–4300.

(11) Wang, Y.; Li, X.; Li, D.; Sun, Y.; Zhang, X. Controllable synthesis of hierarchical SnO_2 microspheres for dye-sensitized solar cells. *J. Power Sources* **2015**, *280*, 476–482.

(12) Kim, M.; Choi, I.; Choi, S.; Song, J.; Mo, S.; An, J.; Jo, Y.; Ahn, S.; Kim, G.; Kim, D. Enhanced electrical properties of Li-salts doped mesoporous TiO_2 in perovskite solar cells. *Joule* **2021**, *5* (3), 659–672.

(13) Jung, H. S.; Park, N. G. Perovskite Solar Cells: From Materials to Devices. *Small* **2015**, *11* (1), 10–25.

(14) Son, D.; Im, J.; Kim, H.; Park, N. 11% efficient perovskite solar cell based on ZnO nanorods: an effective charge collection system. *J. Phys. Chem. C* **2014**, *118* (30), 16567–16573.

(15) Yeom, E. J.; Shin, S. S.; Yang, W. S.; Lee, S. J.; Yin, W.; Kim, D.; Noh, J. H.; Ahn, T. K.; Seok, S. I. Controllable synthesis of single crystalline Sn-based oxides and their application in perovskite solar cells. *J. Mater. Chem. A* **2017**, *5* (1), 79–86.

(16) Zhu, L.; Ye, J.; Zhang, X.; Zheng, H.; Liu, G.; Pan, X.; Dai, S. Performance enhancement of perovskite solar cells using a La-doped $BaSnO_3$ electron transport layer. *J. Mater. Chem. A* **2017**, *5* (7), 3675–3682.

(17) Bera, A.; Wu, K.; Sheikh, A.; Alarousu, E.; Mohammed, O. F.; Wu, T. Perovskite oxide $SrTiO_3$ as an efficient electron transporter for hybrid perovskite solar cells. *J. Phys. Chem. C* **2014**, *118* (49), 28494–28501.

(18) Liu, J.; Gao, C.; Luo, L.; Ye, Y. Q.; He, X.; Yang, L. O.; Guo, X.; Zhuang, D.; Liao, C.; Mei, J.; Lau, L. W. M. Low-temperature, solution processed metal sulfide as an electron transport layer for efficient planar perovskite solar cells. *J. Mater. Chem. A* **2015**, *3* (22), 11750–11755.

(19) Dunlap-Shohl, W. A.; Younts, R.; Gautam, B.; Gundogdu, K.; Mitzi, D. B. Effects of Cd diffusion and doping in high-performance perovskite solar cells using CdS as electron transport layer. *J. Phys. Chem. C* **2016**, *120* (30), 16437–16445.

(20) Wang, K.; Shi, Y.; Dong, Q.; Li, Y.; Wang, S.; Yu, X.; Wu, M.; Ma, T. Low-temperature and solution-processed amorphous WO_X as electron-selective layer for perovskite solar cells. *J. Phys. Chem. Lett.* **2015**, *6* (5), 755–759.

(21) Qin, M.; Ma, J.; Ke, W.; Qin, P.; Lei, H.; Tao, H.; Zheng, X.; Xiong, L.; Liu, Q.; Chen, Z.; Lu, J.; Yang, G.; Fang, G. Perovskite solar cells based on low-temperature processed indium oxide electron selective layers. *ACS Appl. Mater. Interfaces.* **2016**, *8* (13), 8460–8466.

(22) Kogo, A.; Numata, Y. H.; Ikegami, M.; Miyasaka, T. Nb_2O_5 blocking layer for high open-circuit voltage perovskite solar cells. *Chem. Lett.* **2015**, *44* (6), 829–830.

(23) Wang, X.; Deng, L. L.; Wang, L. Y.; Dai, S. M.; Xing, Z.; Zhan, X. X.; Lu, X. Z.; Xie, S. Y.; Huang, R. B.; Zheng, L. S. Cerium oxide standing out as an electron transport layer for efficient and stable perovskite solar cells processed at low temperature. *J. Mater. Chem. A* **2017**, *5* (4), 1706–1712.

(24) Yoo, J. J.; Seo, G.; Chua, M. R.; Park, T. G.; Lu, Y.; Rotermund, F.; Kim, Y.; Moon, C. S.; Jeon, N. J.; Correa-Baena, J.; Bulović, V.; Shin, S. S.; Bawendi, M. G.; Seo, J. Efficient perovskite solar cells via improved carrier management. *Nature* **2021**, *590* (7847), 587–593.

(25) Yeom, E. J.; Shin, S. S.; Yang, W. S.; Lee, S. J.; Yin, W.; Kim, D.; Noh, J. H.; Ahn, T. K.; Seok, S. I. Controllable Synthesis of Single Crystalline Sn-based Oxides and Their Application to Perovskite Solar Cells. *J. Mater. Chem. A* **2017**, *5* (1), 79–86.

(26) Yang, G.; Chen, C.; Yao, F.; Chen, Z.; Zhang, Q.; Zheng, X.; Ma, J.; Lei, H.; Qin, P.; Xiong, L.; Ke, W.; Li, G.; Yan, Y.; Fang, G. Effective carrier-concentration tuning of SnO_2 quantum dot electron-selective layers for high-performance planar perovskite solar cells. *Adv. Mater.* **2018**, *30*, 1706023.

(27) Lama, J.; Chenb, J.; Tsaia, P.; Hsiehb, Y.; Chueh, C.; Tung, S.; Chen, W. A stable, efficient textile-based flexible perovskite solar cell with improved washable and deployable capabilities for wearable device applications. *RSC Adv.* **2017**, *7*, 54361–54368.

(28) Li, Y.; Zhu, J.; Huang, Y.; Liu, F.; Lv, M.; Chen, S. H.; Hu, L. H.; Tang, J. W.; Yao, J. X.; Dai, S. Y. Mesoporous SnO_2 nanoparticle films as electron-transporting material in perovskite solar cells. *RSC Adv.* **2015**, *5*, 28424.

(29) Ke, W.; Fang, G.; Liu, Q.; Xiong, L.; Qin, P.; Tao, H.; Wang, J.; Lei, H.; Li, B.; Wan, J.; Yang, G.; Yan, Y. Low-temperature solution-processed tin oxide as an alternative electron transporting layer for efficient perovskite solar cells. *J. Am. Chem. Soc.* **2015**, *137* (21), 6730–6733.

(30) Anaraki, E. H.; Kermanpur, A.; Steier, L.; Domanski, K.; Matsui, T.; Tress, W.; Saliba, M.; Abate, A.; Gratzel, M.; Hagfeldt, A.; Correa-Baena, J. Highly efficient and stable planar perovskite solar cells by solution-processed tin oxide. *Energy Environ. Sci.* **2016**, *9* (10), 3128–3134.

(31) Jiang, Q.; Zhao, Y.; Zhang, X.; Yang, X.; Chen, Y.; Chu, Z.; Ye, Q.; Li, X.; Yin, Z.; You, J. Surface passivation of perovskite film for efficient solar cells. *Nat. Photonics.* **2019**, *13* (7), 460.

(32) Dong, Q.; Shi, Y.; Zhang, C.; Wu, Y.; Wang, L. Energetically favored formation of SnO_2 nanocrystals as electron transfer layer in perovskite solar cells with high efficiency exceeding 19%. *Nano Energy.* **2017**, *40*, 336–344.

(33) Jiang, Q.; Zhang, L.; Wang, H.; Yang, X.; Meng, J.; Liu, H.; Yin, Z.; Wu, J.; Zhang, X.; You, J. Enhanced electron extraction using SnO_2 for high-efficiency planar-structure $HC(NH_2)_2PbI_3$-based perovskite solar cells. *Nat. Energy* **2017**, *2* (1), 16177.

(34) Zhang, S.; Su, J.; Lin, Z.; Tian, K.; Guo, X.; Zhang, J.; Chang, J.; Hao, Y. Beneficial Role of Organolead Halide Perovskite $CH_3NH_3PbI_3/SnO_2$ Interface: Theoretical and Experimental Study. *Adv. Mater. Interfaces.* **2019**, *6* (17), 1900400.

(35) Du, J.; Feng, L.; Guo, X.; Huang, X.; Lin, Z.; Su, J.; Hu, Z.; Zhang, J.; Chang, J.; Hao, Y. Enhanced efficiency and stability of planar perovskite solar cells by introducing amino acid to SnO_2/perovskite interface. *J. Power Sources* **2020**, *455*, 227974.

(36) Kim, J.; Kim, K. S.; Myung, C. W. Efficient electron extraction of SnO2 electron transport layer for lead halide perovskite solar cell. *NPJ. Comput. Mater.* **2020**, *6*, 100.

(37) Kresse, G.; Hafner, J. Ab initio molecular dynamics for open-shell transition metals. *Phys. Rev. B* **1993**, *48* (17), 13115–13118.

(38) Kresse, G.; Furthmüller, J. Efficient iterative schemes for ab initio total-energy calculations using a plane-wave basis set. *Phys. Rev. B* **1996**, *54* (16), 11169.

(39) Blöchl, P. E. Projector augmented-wave method. *Phys. Rev. B* **1994**, *50* (24), 17953.

(40) Kresse, G.; Joubert, D. From ultrasoft pseudopotentials to the projector augmented-wave method. *Phys. Rev. B* **1999**, *59* (3), 1758.

(41) Grimme, S. Semiempirical GGA-type density functional constructed with a long-range dispersion correction. *J. comput. chem.* **2006**, *27* (15), 1787–1799.

(42) Perdew, J. P.; Burke, K. M. Ernzerhof. Generalized gradient approximation made simple. *Phys. Rev. Lett.* **1996**, *77* (18), 3865.

(43) Heyd, J.; Scuseria, G. E.; Ernzerhof, M. Hybrid functionals based on a screened Coulomb potential. *J. Chem. Phys.* **2003**, *118* (18), 8207–8215.

(44) Geng, W.; Zhang, L.; Zhang, Y. N.; Lau, W. M.; Liu, L. M. First-principles study of lead iodide perovskite tetragonal and orthorhombic phases for photovoltaics. *J. Phys. Chem. C* **2014**, *118* (34), 19565–19571.

(45) Poglitsch, A.; Weber, D. Dynamic disorder in methylammoniumtrihalogenoplumbates (II) observed by millimeter-wave spectroscopy. *J. Chem. Phys.* **1987**, *87* (11), 6373−6378.

(46) Baikie, T.; Fang, Y.; Kadro, J. M.; Schreyer, M.; Wei, F.; Mhaisalkar, S. G.; Graetzel, M.; White, T. J. Synthesis and crystal chemistry of the hybrid perovskite $(CH_3NH_3)PbI_3$ for solid-state sensitised solar cell applications. *J. Mater. Chem. A* **2013**, *1* (18), 5628−5641.

(47) Haines, J.; Léger, J. M. X-ray diffraction study of the phase transitions and structural evolution of tin dioxide at high pressure: ffRelationships between structure types and implications for other rutile-type dioxides. *Phys. Rev. B* **1997**, *55* (17), 11144.

(48) Cai, X.; Zhang, P.; Wei, S. H. Revisit of the band gaps of rutile SnO_2 and TiO_2: a first-principles study. *J. Semicond.* **2019**, *40* (9), No. 092101.

(49) Haruyama, J.; Sodeyama, K.; Han, L.; Tateyama, Y. Termination dependence of tetragonal $CH_3NH_3PbI_3$ surfaces for perovskite solar cells. *J. Phys. Chem. Lett.* **2014**, *5* (16), 2903−2909.

(50) Xiao, W.; Pu, W. H.; Wang, J. W.; Sun, L.; Cui, J. D.; Wang, L. G. Theoretical investigation of the structural and electronic properties of Al-decorated TiO_2/perovskite interfaces. *Appl. Surf. Sci.* **2019**, *492*, 369−373.

(51) Xiao, W.; Wang, J. N.; Wang, J. W.; Huang, G. J.; Cheng, L.; Jiang, L. J.; Wang, L. G. Structural and electronic properties of the heterointerfaces for Cu_2ZnSnS_4 photovoltaic cells: a densityfunctional theory study. *Phys. Chem. Chem. Phys.* **2016**, *18* (17), 12029.

(52) Zhang, S.; Su, J.; Lin, Z.; Tian, K.; Guo, X.; Zhang, J.; Chang, J.; Hao, Y. Beneficial role of organolead halide perovskite $CH_3NH_3PbI_3$/SnO_2 interface: theoretical and experimental study. *Adv. Mater. Interfaces* **2019**, *6* (17), 1900400.

(53) Jiang, Q.; Zhang, X.; You, J. SnO_2: a wonderful electron transport layer for perovskite solar cells. *Small* **2018**, *14* (31), 1801154.

(54) Geng, W.; Tong, C.; Liu, J.; Zhu, W.; Lau, W.; Liu, L. Structures and electronic properties of different $CH_3NH_3PbI_3$/TiO_2 interface: a first-principles study. *Sci. Rep.* **2016**, *6* (1), 20131.

(55) Wei, S.; Zunger, A. Calculated natural band offsets of all II−VI and III−V semiconductors: Chemical trends and the role of cation d orbitals. *Appl. Phys. Lett.* **1998**, *72* (16), 2011−2013.

(56) Li, Y.; Walsh, A.; Chen, S.; Yin, W.; Yang, J.; Li, J.; Silva, J. L. F. D.; Gong, X. G.; Wei, S. Revised ab initio natural band offsets of all group IV, II-VI, and III-V semiconductors. *Appl. Phys. Lett.* **2009**, *94*, 212109.

(57) Correa Baena, J. P.; Steier, L.; Tress, W.; Saliba, M.; Neutzner, S.; Matsui, T.; Giordano, F.; Jacobsson, T. J.; Srimath Kandada, A. R.; Zakeeruddin, S. M.; Petrozza, A.; Abate, A.; Nazeeruddin, M. K.; Gratzel, M.; Hagfeldt, A. Highly efficient planar perovskite solar cells through band alignment engineering. *Energy Environ. Sci.* **2015**, *8* (10), 2928−2934.

(58) Zhao, J.; Zhang, Y.; Zhao, X.; Zhang, J.; Wang, H.; Zhu, Z.; Liu, Q. Band alignment strategy for printable triple mesoscopic perovskite solar cells with enhanced photovoltage. *ACS Appl. Energy Mater.* **2019**, *2* (3), 2034−2042.

(59) Wang, S.; Luo, Q.; Fang, W.; Long, R. Interfacial Engineering Determines Band Alignment and Steers Charge Separation and Recombination at an Inorganic Perovskite Quantum Dot/WS_2 Junction: A Time Domain Ab Initio Study. *J. Phys. Chem. Lett.* **2019**, *10* (6), 1234−1241.

(60) Park, M.; Kim, J.; Son, H. J.; Lee, C.; Jang, S. S.; Ko, M. J. Low-temperature solution-processed Li-doped SnO_2 as an effective electron transporting layer for high-performance flexible and wearable perovskite solar cells. *Nano Energy* **2016**, *26*, 208−215.

(61) Wang, C.; Zhao, D.; Grice, C. R.; Liao, W.; Yu, Y.; Cimaroli, A.; Shrestha, N.; Roland, P. J.; Chen, J.; Yu, Z.; Liu, P.; Cheng, N.; Ellingson, R. J.; Zhao, X.; Yan, Y. Low-temperature plasma-enhanced atomic layer deposition of tin oxide electron selective layers for highly efficient planar perovskite solar cells. *J. Mater. Chem. A* **2016**, *4* (31), 12080−12087.

(62) Yang, D.; Yang, R.; Wang, K.; Wu, C.; Zhu, X.; Feng, J.; Ren, X.; Fang, G.; Priya, S.; Liu, S. High efficiency planar-type perovskite solar cells with negligible hysteresis using EDTA-complexed SnO_2. *Nat. Commun.* **2018**, *9* (1), 3239.

(63) Xiong, L. B.; Qin, M. C.; Chen, C.; Wen, J.; Yang, G.; Guo, Y. X.; Ma, J. J.; Jiang, Q.; Qin, P. L.; Li, S. Z.; Fang, G. F. Fully High-Temperature-Processed SnO_2 as Blocking Layer and Scaffold for Efficient, Stable, and Hysteresis-Free Mesoporous Perovskite Solar Cells. *Adv. Funct. Mater.* **2018**, *28*, 1706276.

(64) Wu, J.; Cui, Y.; Yu, B.; Liu, K.; Li, Y.; Li, H.; Shi, J.; Wu, H.; Luo, Y.; Li, D.; Meng, Q. A simple way to simultaneously release the interface stress and realize the inner encapsulation for highly efficient and stable perovskite solar cells. *Adv. Funct. Mater.* **2019**, *29* (49), 1905336.

(65) Bi, H.; Liu, B.; He, D.; Bai, L.; Wang, W.; Zang, Z.; Chen, J. Interfacial defect passivation and stress release by multifunctional KPF_6 modification for planar perovskite solar cells with enhanced efficiency and stability. *Chem. Eng. J.* **2021**, *418*, 129375.

(66) Yin, W. J.; Shi, T.; Yan, Y. Unusual defect physics in $CH_3NH_3PbI_3$ perovskite solar cell absorber. *Appl. Phys. Lett.* **2014**, *104* (6), No. 063903.

(67) Freeman, C. M.; Catlow, C. R. A. A computer modeling study of defect and dopant states in SnO_2. *J. Solid State Chem.* **1990**, *85* (1), 65−75.

(68) Mohamad Noh, M. F.; Arzaee, N. A.; Safaei, J.; Mohamed, N. A.; Kim, H. P.; Mohd Yusoff, A. R.; Jang, J.; Mat Teridi, M. A. Eliminating oxygen vacancies in SnO_2 films via aerosol-assisted chemical vapour deposition for perovskite solar cells and photoelectrochemical cells. *J. Alloys Compd.* **2019**, *773*, 997−1008.

(69) Shi, T.; Zhang, H. S.; Meng, W.; Teng, Q.; Liu, M.; Yang, X.; Yan, Y.; Yip, H. L.; Zhao, Y. J. Effects of organic cations on the defect physics of tin halide perovskites. *J. Mater. Chem. A* **2017**, *5* (29), 15124−15129.

(70) Khadka, D. B.; Khadka, D. B.; Shirai, Y.; Yanagida, M.; Noda, T.; Miyano, K. Tailoring the open-circuit voltage deficit of wide-band-gap perovskite solar cells using alkyl chain-substituted fullerene derivatives. *ACS appl. Mater. Interfaces* **2018**, *10* (26), 22074−22082.

(71) Yin, W. J.; Shi, T.; Yan, Y. Unique properties of halide perovskites as possible origins of the superior solar cell performance. *Adv. Mater.* **2014**, *26* (27), 4653−4658.

(72) Zhong, Y.; Hufnagel, M.; Thelakkat, M.; Li, C.; Huettner, S. Role of PCBM in the suppression of hysteresis in perovskite solar cells. *Adv. Funct. Mater.* **2020**, *30* (23), 1908920.

(73) Zhou, X.; Qi, W.; Li, J.; Cheng, J.; Li, Y.; Luo, J.; Ko, M. J.; Li, Y.; Zhao, Y.; Zhang, X. Toward Efficient and Stable Perovskite Solar Cells: Choosing Appropriate Passivator to Specific Defects. *Sol. RRL* **2020**, *4* (10), 2000308.